Flow recession behavior of preferential subsurface flow patterns with minimum energy dissipation

Jannick Strüven[1] and Stefan Hergarten[1]

[1]Institut für Geo- und Umweltnaturwissenschaften, Albertstr. 23B, 79104 Freiburg, Germany

Correspondence: Jannick Strüven
(jannick.strueven@geologie.uni-freiburg.de)

Abstract. Understanding the properties of preferential flow patters is a major challenge in subsurface hydrology. Most of the theoretical approaches in this field stem from research on karst aquifers, where typically two or three distinct flow components with different time scales are considered. This study starts from a different concept, where a continuous spatial variation in transmissivity and storativity over several orders of magnitude is assumed. Distribution and spatial pattern of these properties are derived from the concept of minimum energy dissipation. While the numerical simulation of such systems is challenging, it is found that a reduction to a dendritic flow pattern, similar to rivers at the surface, works well. It is also shown that spectral theory is useful for investigating the fundamental properties of such aquifers. As a main result, the long-term recession of the spring draining the aquifer during periods of drought becomes slower for large catchments. However, the dependence of the respective recession coefficient on catchment size is much weaker than for homogeneous aquifers. Concerning the short-term behavior after an instantaneous recharge event, strong deviations from the exponential recession of a linear reservoir are observed. In particular, it takes a considerable time span until the spring discharge reaches its peak. This rise time is in an order of magnitude of one-seventh of the e-folding recession time. Despite the strong deviations from the linear reservoir at short times, the exponential component typically contributes more than 80 % to the total discharge. This fraction is much higher than expected for karst aquifers and even exceeds the fraction predicted for homogeneous aquifers.

1 Introduction

The recession of spring discharge after recharge events can be seen as the fingerprint of an aquifer. In contrast to pumping tests at wells, it is a passive method based on data that are often recorded routinely. Additionally, spring discharges depend on the overall properties of the catchment, while pumping tests reflect the properties in a region around the well.

More than a century ago, Maillet (1905) proposed the linear reservoir where discharge Q is directly proportional to the stored volume V,

$$Q(t) = \alpha V(t). \tag{1}$$

The linear reservoir is described by a single parameter α [s^{-1}] and the stored volume follows the ordinary differential equation

$$\frac{d}{dt}V(t) = -Q(t) + R(t) = -\alpha V(t) + R(t), \tag{2}$$

where $R(t)$ [m^{3}s^{-1}] is the recharge. During periods with zero recharge, both the stored volume and the discharge decay exponentially with the same decay constant α, also called recession coefficient,

$$V(t) = V(0)e^{-\alpha t}, \tag{3}$$

$$Q(t) = Q(0)e^{-\alpha t}. \tag{4}$$

The inverse of the recession coefficient, $\tau = \frac{1}{\alpha}$, defines the e-folding time, so the time interval over which the discharge decreases by a factor of e.

The linear reservoir is not only appealing because it can be described by a single parameter, but even more because its behavior during periods of drought depends only on the actual amount of water, but is independent of the recharge history. It often provides a reasonable approximation for long periods of drought. Deviations from the exponential decay at shorter time scales have been investigated and used for characterizing aquifers since the 1960s, where in particular karst systems have been addressed in numerous studies and several theoretical concepts were proposed.

Forkasiewicz and Paloc (1967) suggested a superposition of three distinct linear reservoirs with different decay constants describing three major flow components – a network of highly conductive conduits, an intermediate system of well integrated fissures, and a network of pores or narrow fissures with low permeability. The behavior of this model is dominated by the slowest reservoir during long periods of drought.

Mangin (1975) introduced a different approach using two components. The slow component was described as a linear reservoir, and a fast component with a limited range was added. The parameters of the fast components are the basis of the widely used karst classification system suggested in the same study. Several other modeling approaches which are similar in their spirit were developed (e.g., Drogue, 1972; Atkinson, 1977; Padilla et al., 1994; Kovács and Perrochet, 2014; Xu et al., 2018; Basha, 2020; Kovács, 2021). Beyond these approaches, a multitude of numerical models designed for simulating real-world scenarios is nowadays availaible. For deeper insights, readers are referred to the review paper by Fiorillo (2014) and to the model comparison by Jeannin et al. (2021).

While deviations from the linear reservoir are particular relevant for karst systems, it should be noted that even the simplest Darcy-type aquifers are not linear reservoirs. Assuming a given transmissivity T [m^{2}s^{-1}] and a given storativity S [-], the simplest Darcy-type aquifer is described by the water balance equation

$$S\frac{\partial h}{\partial t} = -\text{div}\,\boldsymbol{q} + r, \tag{5}$$

where h [m] is the hydraulic head,

$$\boldsymbol{q} = -T\nabla h, \tag{6}$$

[m^{2}s^{-1}] the 2-D flux density (volume per time and cross section width), ∇ the 2-D gradient operator, r the recharge per area [ms^{-1}], and div the 2-D divergence operator. Inserting Eq. (6) into Eq. (5) yields a partial differential equation of the diffusion type for the hydraulic head h,

$$S\frac{\partial h}{\partial t} = \text{div}\left(T\nabla h\right) + r. \tag{7}$$

This model was investigated in several studies for constant T and S in square or rectangular domains (e.g., Rorabaugh, 1964; Nutbrown, 1975; Kovács et al., 2005; Kovács and Perrochet, 2008). Applying spectral theory (see Sect. 2.4), it was shown that the total discharge Q (q integrated over the entire boundary) can be described by an infinite series of exponential terms with different decay constants during periods of drought. Since the term with the smallest decay constant dominates at large times, the behavior approaches that of the linear reservoir. However, the question how well the linear reservoir approximates the properties of real aquifers practically or whether the linear reservoir is even some kind of preferred state from a theoretical point of view, has been discussed controversially (e.g., Fenicia et al., 2006; de Rooij, 2014; Kleidon and Savenije, 2017; Savenije, 2018).

Including the early recession phase in the analysis yields more information about the aquifer, but increases the dependence of the results on the recharge history in turn. The instantaneous unit hydrograph, which dates back to concepts of Sherman (1932), is widely used in this context. It describes the discharge arising from a unit amount of recharge that is applied instantaneously at $t = 0$ over the entire domain.

The unit hydrograph of the simple Darcy aquifer differs strongly from that of the linear reservoir and as well as from the empirical approaches proposed by Forkasiewicz and Paloc (1967) and by Mangin (1975). While these models predict a finite discharge at $t = 0$, it diverges according to a power law,

$$Q(t) \propto t^{-\frac{1}{2}}, \tag{8}$$

in the limit $t \to 0$ for the simple Darcy aquifer (e.g., Hergarten and Birk, 2007). Such a power-law decrease also occurs in models consisting of porous blocks connected by highly conductive conduits (Kovács et al., 2005; Kovács and Perrochet, 2008). However, a finite conductance of the conduits limits the power-law divergence at short times (Kovács and Perrochet, 2014). Hergarten and Birk (2007) extended this concept by a fractal distribution of block sizes. While this model was able to explain a power-law recession with exponents different from $-\frac{1}{2}$, deriving aquifer properties from the power-law behavior of recession curves turned out to be challenging. Birk and Hergarten (2010) investigated synthetic hydrographs for recharge events of finite duration and found that the properties of the recharge event likely obscure the short-term dynamics of the porous blocks.

The quantification of heterogeneity and its representation in numerical models are still major challenges in hydrology. Carbonatic aquifers are particularly interesting in this context due to the interplay fluid flow and structure. The spatial structure of the aquifer has a strong influence on fluid flow, which in turn controls dissolution and precipitation and thus also the long-term change of the structure. This interaction has been addressed in modeling studies of binary karst systems consisting of a porous medium and discrete conduits (e.g., Kaufmann and Braun, 2000; Birk et al., 2003; Kaufmann et al., 2010) as well as in

the context of continuous changes in porosity and conductivity (e.g., Edery et al., 2021). Similar processes can also take place in soils by subsurface erosion (e.g., Bernatek-Jakiel and Poesen, 2018).

As an alternative to forward modeling, there is an increasing number of studies attempting to derive preferred states of the atmosphere and the hydrosphere from principles of optimality (e.g., Kleidon and Schymanski, 2008; Kleidon and Renner, 2013; Kleidon et al., 2014; Kleidon and Savenije, 2017; Kleidon et al., 2019; Zehe et al., 2010, 2013, 2021; Westhoff and Zehe, 2013; Westhoff et al., 2014, 2017; Zhao et al., 2016; Schroers et al., 2022). In the context of fluid flow, minimum energy dissipation seems to be a promising concept, which was successfully applied to river networks (Howard, 1990; Rodriguez-Iturbe et al., 1992a, b; Rinaldo et al., 1992; Maritan et al., 1996) and to the cardiovascular system of mammals (West et al., 1997; Enquist et al., 1998, 1999; Banavar et al., 1999; West et al., 1999a, b).

Hergarten et al. (2014) developed a theory for an optimal spatial distribution of porosity and hydraulic conductivity in the sense that the total energy dissipation of the flow is minimized. As a major difference towards the studies focusing on karst systems mentioned above, this theory does not predict a binary or ternary system of distinct flow components, but a continuous variation in the hydraulic properties over several orders of magnitude in combination with a highly organized spatial pattern. The predicted spatial pattern is dendritic and similar to drainage networks at the surface. So it does not capture the variety of preferential flow patterns found in nature entirely.

The potential relation of this theoretical concept to subsurface hydrology is still unclear. Validation is limited to the statistical distribution of catchment sizes and leaves several open questions (Hergarten et al., 2016). Even the properties of the model have not been analyzed thoroughly, except for residence times in a steady state (Hergarten et al., 2014).

This study investigates the dynamic properties of such preferential flow patterns based on the instantaneous unit hydrograph. The main research question is how preferential flow patterns with minimum energy dissipation are related to the different concepts discussed above. In more detail: How much does their behavior differ from that of a homogeneous aquifer or a linear reservoir? Can we explain the typical behavior of karst springs without assuming two or three distinct flow components? On which physical properties do short- and long-term properties of such an aquifer depend on?

2 Approach

2.1 Linearized consideration

The instantaneous unit hydrograph describes the response of an aquifer to adding a unit amount of water instantaneously. It is particularly useful for linear systems since the response to any recharge curve $r(t)$ can be obtained by superposing multiple recharge events at different times (formally, the convolution integral of $r(t)$ and the instantaneous unit hydrograph).

For unconfined aquifers, however, the transmissivity is proportional to the height of the water column,

$$T = K(h - b), \tag{9}$$

where K is the hydraulic conductivity [$\mathrm{m\,s^{-1}}$] and b the base of the aquifer [m]. Since this dependence introduces a nonlinearity in Eq. (7), we can only make use of the linear theory for small disturbances. For this, we assume a steady state at a recharge r_0

and apply a small additional recharge δr, so that $r = r_0 + \delta r$. Then we can write the actual head in the form $h = h_0 + \delta h$ with the steady-state head h_0. Equation (5) retains its shape,

$$S\frac{\partial \delta h}{\partial t} = -\text{div}\boldsymbol{\delta q} + \delta r, \tag{10}$$

but with

$$\boldsymbol{\delta q} \quad = \quad -K\left((h_0 + \delta h - b)\nabla(h_0 + \delta h) + (h_0 - b)\nabla h_0\right) \tag{11}$$

$$\approx \quad -K\left((h_0 - b)\nabla\delta h + \delta h \nabla h_0\right) \tag{12}$$

for small δh. The first term is the effect of a change in the hydraulic gradient at constant transmissivity $T_0 = K(h_0 - b)$, which has the same form as Eq. (6). The second term describes the change in flux arising from the change in the thickness of the water column at constant hydraulic gradient. This term is particularly relevant for sloping aquifers with thin water layers.

Since the concept developed in the following only captures the first term, the second term is neglected in this study. This means that the steady-state water table should be almost horizontal and the respective water column should not be too thin. In this case (neglecting the second term in Eq. 12), δh is decribed by the same equation as h in Eq. (7), but with δr and $T = T_0$. For simplicity, δh, $\boldsymbol{\delta q}$, and δr are labeled h, $\boldsymbol{q}$, and r, respectively. So we have to keep in mind that these properties are not absolute values, but small deviations from a steady state. Furthermore, T is the steady-state transissivity T_0 in the following.

2.2 Basic setup

Following the considerations of the previous section, we consider a 2-D aquifer with a given transmissivity T [m^{2}s^{-1}] and a given storativity S [-], described by Eqs. (5) and (6). Since focus is on strongly organized preferential flow patterns, both T and S are not spatially uniform, but may even vary over several orders of magnitude. As discussed in the previous section, the head values h, the flux density $\boldsymbol{q}$, and the recharge r are not absolute values, but deviations from a steady state. As the simplest boundary condition, it can be assumed that the hydraulic head at springs remains constant, which is equivalent to the boundary condition $h = 0$.

On a regular grid with a uniform grid spacing d, Eqs. (5) and (6) can be discretized by a finite-volume approach according to

$$d^2 S_i \frac{\partial h_i}{\partial t} = -\sum_{j \in N(i)} q_{ij} + d^2 r_i \tag{13}$$

with the fluxes

$$q_{ij} = dT_{ij}\frac{h_i - h_j}{d}. \tag{14}$$

The nodes of the grid were numbered by a single index i, where $N(i)$ denotes the nearest neighborhood of the node i, consisting of four neighbors except for boundary nodes. The symbol q_{ij} [m^{2}s^{-1}] refers to the flux from the node i to the node j, while T_{ij} is the respective transmissivity. Note that q_{ij} already includes the length of the edge between the two nodes (first term d

in Eq. 14), so that it is no longer a flux per unit width. Inserting Eq. (14) into Eq. (13) yields the respective discrete form of Eq. (7).

Solving this equation numerically on large grids is challenging if the transmissivity varies over several orders of magnitude. Using an explicit scheme for the timestep requires very small time increments since small changes in hydraulic head cause large fluxes. Employing a fully implicit scheme overcomes this limitation since fully implicit schemes are stable at arbitrary time increments for diffusion-type equations. However, most of the available algorithms for solving the resulting linear equation system do not perform well if T varies strongly. This also applies to multigrid schemes (e.g., Hackbusch, 1985), which are the only schemes with linear time complexity, so where the numerical effort per time step increases only linearly with the number of nodes.

2.3 Dendritic flow patterns

The theory of minimum energy dissipation in Darcy flow proposed by Hergarten et al. (2014) approximates preferential flow patterns by dendritic structures. This means that each node i delivers its entire discharge to one of its neighbors, b, called flow target in the following (strictly speaking, it should be labeled b_i). The flow target is defined as the neighbor with the steepest descent in hydraulic head, which is the same as the neighbor with the lowest head value for a grid with uniform spacing in both directions. Then, the neighborhood consists of three groups of nodes: (i) One flow target. (ii) Some neighbors that deliver their discharge to the considered node, called donors in the following. (iii) Some nodes that do not interact with the considered node. The last group of nodes makes the difference towards the original model where all neighbored nodes interact.

Since we consider only small deviations from a steady state, we can assume that the topology of the flow pattern does not change through time. The flow target of each node is determined from the steady state and persists. As a major advantage, this simplification inhibits the occurrence of nodes without a flow target.

The discrete version of the balance equation (Eq. 13) turns into

$$d^2 S_i \frac{\partial h_i}{\partial t} = -q_i + \sum_{j \in D(i)} q_j + d^2 r_i \tag{15}$$

for a dendritic flow pattern, where the notation q_i (with a single index) describes the flux from the node i to its flow target (so q_{ib} in the general notation). The sum extends over all donors of the node i, denoted $D(i)$ here.

Since the topology of the flow pattern is static, the head value of a node may become lower than that of its flow target, in which case Eq. (14) predicts a negative flux. In the context of small deviations from a steady state, a negative flux would not have an immediate meaning since it just says that the flux towards the flow target is lower than in the steady state. However, there is no problem even if backward flux occurs on an absolute scale.

Dendritic networks are widely used in the context of surface flow patterns, in particular river networks at large scales. In order to reduce effects of anisotropy, the so-called D8 scheme is typically used on a regular, two-dimensional grid. Here, 8 neighbors (4 nearest neighbors and 4 diagonal neighbors) are considered, so that river segments are either parallel to one of the coordinate axes or diagonal. While the numerical construction of optimized drainage patters by Hergarten et al. (2014) also used the D8 scheme, we consider only the 4 nearest neighbors (D4 scheme) in the following. The main reason for this

limitation is the comparison to the original model in Sect. 3.1. The D4 scheme can be seen as a restriction of the original model, while the D8 version would allow for additional flow paths. In particular, a diagonal line of points with a high transmissivity would be a preferential flow path with regard to the D8 scheme, but not in the original model.

While the concept of dendritic flow patterns was used by Hergarten et al. (2014) for constructing patterns of porosity and conductivity (see also Sect. 2.7), recent developments in numerics make this concept interesting for time-dependent modeling. In the following sections, two numerical approaches that are robust against strong variations in transmissivity are presented.

2.4 Spectral theory

Large parts of this study are based on spectral theory. Spectral theory decomposes the solution into a set of functions with a simple behavior. The functions are simple in the sense that they can be written in the form

$$h(\boldsymbol{x},t) = h(\boldsymbol{x},0)f(t), \tag{16}$$

which means that their shape does not change through time. For $r = 0$, Eq. (7) can then be separated into one equation for $h(\boldsymbol{x},0)$ and another equation for the time dependence $f(t)$. This result is recognized by inserting $h(\boldsymbol{x},t)$ into Eq. (7) and dividing both sides by $h(\boldsymbol{x},t)$ and by S, which yields

$$\frac{\frac{d}{dt}f(t)}{f(t)} = \frac{\frac{1}{S}\mathrm{div}\,(T\nabla h(\boldsymbol{x},0))}{h(\boldsymbol{x},0)}. \tag{17}$$

Since the left-hand side is independent of $\boldsymbol{x}$ and the right-hand side is independent of t, both sides must be constant. If we call the respective constant $-\alpha$, the solution for f is

$$f(t) = e^{-\alpha t} \tag{18}$$

since Eq. (16) requires $f(0) = 1$. So

$$h(\boldsymbol{x},t) = h(\boldsymbol{x},0)e^{-\alpha t} \tag{19}$$

decreases exponentially for $\alpha > 0$ and increases for $\alpha < 0$. The right-hand side of Eq. (17) yields the eigenvalue equation

$$-\frac{1}{S}\mathrm{div}\,(T\nabla h) = \alpha h. \tag{20}$$

for $h(\boldsymbol{x},0)$. This means that the differential operator $-\frac{1}{S}\mathrm{div}T\nabla$ applied to the function h just multiplies h by the factor α. Mathematically, h is an eigenfunction of the differential operator and α the respective eigenvalue.

While the eigenfunctions and the respective eigenvalues can be computed analytically for some simple geometries (e.g., Rorabaugh, 1964; Nutbrown, 1975; Kovács et al., 2005; Kovács and Perrochet, 2008, for rectangular domains) and constant parameters, a heterogeneous distribution of S and T requires a numerical treatment. The numerical treatment requires a transition from the continuous function h to the values h_i on the discrete grid. Using the same finite volume discretization as above (Eqs. 13 and 14), the term $-\frac{1}{S}\mathrm{div}\,(T\nabla h)$ can be approximated at the i-th node by

$$-\frac{1}{S}\mathrm{div}\,(T\nabla h)\bigg|_i \approx \frac{1}{S_i}\sum_{j\in N(i)} T_{ij}(h_i - h_j), \tag{21}$$

where unit grid spacing ($d = 1$) was assumed for simplicity. Aligning all values h_i in a column vector, this relation can be written in matrix form

$$-\frac{1}{S}\text{div}\,(T\nabla h) \approx Ah \tag{22}$$

with a square matrix A. It is easily recognized that the nondiagonal elements of A are

$$A_{ij} = \begin{cases} -\frac{T_{ij}}{S_i} & \text{for } j \in N(i) \\ 0 & \text{else} \end{cases}, \tag{23}$$

while the diagonal elements are

$$A_{ii} = \sum_{j \in N(i)} (-A_{ij}) = \sum_{j \in N(i)} \frac{T_{ij}}{S_i}. \tag{24}$$

This matrix is the same as needed for solving the steady-state version of Eq. (7) numerically. The respective form of the matrix for dendritic flow patterns is basically the same, where only the neighborhood has to be reduced to those points that are connected, i.e., where either j is the flow target of i or vice versa.

Since all software packages for linear algebra provide functions for computing eigenvalues, the steps are technically not very challenging up to this point. However, each eigenvalue and the respective eigenfunction is just one solution of Eq. (7) with $r = 0$ for a specific initial condition $h(\boldsymbol{x}, 0)$. In turn, we need the solution for any given initial condition. Spectral theory expresses a given initial condition as a superposition of eigenfunctions and then uses the knowledge about the individual eigenfunctions for predicting the full solution.

Let us assume that we computed all eigenfunctions and that e_{ki} is the value of the k-th eigenfunction at the node i. If $h_i(0)$ is the initial value at this node, we need coefficients λ_k so that $h_i(0)$ is the superposition of the respective values e_{ki},

$$h_i(0) = \sum_k \lambda_k e_{ki}. \tag{25}$$

Then the values of h at time t are

$$h_i(t) = \sum_k \lambda_k e_{ki} e^{-\alpha_k t}, \tag{26}$$

where α_k is the k-th eigenvalue of A. So all head values can be written as a sum of exponentially decaying terms, provided that all eigenvalues are positive. The latter can be shown for the matrix defined by Eqs. (23) and (24) with the help of Gershgorin's circle theorem.

Since all head values can be decomposed into a sum of exponential functions, the fluxes and thus also the discharge of a spring can be expressed the same way,

$$Q(t) = \sum_k \lambda_k Q_k e^{-\alpha_k t}, \tag{27}$$

where Q_k is the discharge of the k-th eigenfunction. If we assume that the eigenvalues are sorted in increasing order, the long-term recession coefficient is $\alpha = \alpha_1$.

The nontrivial question is whether each initial condition can be expressed as a superposition of eigenfunctions according to Eq. (25). Mathematically, this property relies on the symmetry of the differential operator or, for the discrete problem, on the symmetry of the matrix ($A_{ij} = A_{ji}$). If A is symmetric, a basis of eigenvectors (the representations of the eigenfunctions on the discrete grid) can be found, which ensures the applicability of Eq. (25) for any initial condition with unique coefficients λ_k.

The symmetry of A even guarantees the existence of an orthonormal basis. As a main advantage, an orthonormal basis allows for computing each coefficient λ_k from the inner product (scalar product) of the initial head distribution and the respective eigenvector. So we can obtain the long-term recession coefficient $\alpha = \alpha_1$ and the contribution of the respective component to the total (time-integrated) discharge from the lowest eigenvalue and the respective eigenvector alone. Otherwise, we would need all eigenvectors. Since their number equals the number of nodes, this would be expensive on large grids and would cost the advantage over a direct forward simulation.

Since T_{ij} is the transmissivity between the nodes i and j, $T_{ij} = T_{ji}$. Without the term S_i in Eq. (23), this property would already guarantee the symmetry of A. With this term, however, A is only symmetric if $S_i = S_j$, so if S is the same everywhere.

To overcome this limitation, we need to get a bit deeper into linear algebra and consider a wider definition of symmetry coming from the concept of linear maps. Here, symmetry is related to an inner product, and the condition for symmetry is

$$Ah \cdot \tilde{h} = h \cdot A\tilde{h}, \tag{28}$$

where $\cdot$ is the inner product. This condition has to be satisfied for all h and $\tilde{h}$. It is easily recognized that the criterion $A_{ij} = A_{ji}$ describes the specific case for the standard scalar product

$$h \cdot \tilde{h} = \sum_i h_i \tilde{h}_i. \tag{29}$$

For deeper insights into the fundamentals, readers are referred to textbooks of linear algebra (e.g., Halmos, 1958).

To proof the symmetry of A in this sense, we need the custom inner product

$$h \cdot \tilde{h} = \sum_i S_i h_i \tilde{h}_i, \tag{30}$$

which differs from the standard scalar product (Eq. 29) by its weighting with the storativity S. Using the definition of A (Eqs. 23 and 24), it is easily recognized that

$$S_i A_{ij} = S_j A_{ji}, \tag{31}$$

and thus

$$(Ah) \cdot \tilde{h} = \sum_i S_i \left(\sum_j A_{ij} h_j \right) \tilde{h}_i \tag{32}$$

$$= \sum_{i,j} S_i A_{ij} h_j \tilde{h}_i \tag{33}$$

$$= \sum_{i,j} S_j A_{ji} h_j \tilde{h}_i \tag{34}$$

$$= \sum_{i,j} S_j h_j \left(\sum_i A_{ji} \tilde{h}_i \right) \tag{35}$$

$$= h \cdot \left(A \tilde{h} \right), \tag{36}$$

which proves the symmetry of A with regard to the custom inner product.

Technically, the normalization of the eigenvectors obtained numerically is the only point that requires attention. The eigenvectors have to be normalized with respect to the custom inner product and not with respect to the standard scalar product, so according to the condition

$$e_k \cdot e_k = \sum_i S_i e_{ki}^2 = 1. \tag{37}$$

If h_i are the head values at $t = 0$, the coefficients λ_k in Eqs. (25) and (26) are then obtained from the inner products in the form

$$\lambda_k = h \cdot e_k = \sum_i S_i h_i e_{ki}. \tag{38}$$

This relation becomes particularly simple for the instantaneous unit hydrograph. Applying a unit amount of water per area to all nodes results in $S_i h_i = 1$ for all i, and thus

$$\lambda_k = \sum_i e_{ki}. \tag{39}$$

So the coefficient λ_k is obtained by adding the head values of the respective normalized eigenfunction at all nodes.

2.5 Forward modeling

Spectral theory is very efficient for characterizing the long-term recession since only the components with the lowest recession coefficients α_k are relevant here. In turn, computing the instantaneous unit hydrograph at short times requires a large number of eigenfunctions, so that the advantage over direct forward modeling is lost. Therefore, we also implemented a numerical scheme for forward modeling of the dendritic model. For this purpose, we adopted the very efficient, fully implicit scheme that was recently proposed in the context of fluvial erosion and sediment transport by Hergarten (2020). As a major advantage, the scheme is robust against strong spatial variations in transmissivity. For simplicity, the scheme is only described for the D4 neighborhood with unit grid spacing ($d = 1$) in the following.

Let us consider a time step from t to $t + \delta t$. Replacing the time derivative at the left-hand side of Eq. (15) by a difference quotient and evaluating the fluxes at the right-hand side at the time $t + \delta t$ (for the fully implicit treatment) yields

$$S_i \frac{h_i(t + \delta t) - h_i(t)}{\delta t} = -q_i(t + \delta t) + \sum_{j \in D(i)} q_j(t + \delta t) + r_i. \tag{40}$$

290 The key idea behind the scheme is that all fluxes respond linearly to changes in h of the flow target b due to the linearity of the differential equation. In particular, the flux $q_i(t + \delta t)$ depends linearly on h_b, so that

$$q_i(t + \delta t) = q_i^0 + q_i' \left(h_b(t + \delta t) - h_b(t) \right). \tag{41}$$

Here, q_i^0 is the hypothetic flux at time $t + \delta t$ under the assumption that h_b remains constant ($h_b(t + \delta t) = h_b(t)$). It is not the same as $q_i(t)$ since q_i may also change if q_b remains constant. The second term in Eq. (41) describes the effect of changes in

295 $h_b(t + \delta t)$ on $q_i(t + \delta t)$ where q_i' is the partial derivative of $q_i(t + \delta t)$ with respect to $h_b(t + \delta t)$.

As shown in Appendix A, q_i^0 and q_i' can be computed from the respective properties of the donors and from the known values of h at time t by the expressions

$$q_i^0 = T_i \frac{\left(\frac{S_i}{\delta t} - \sum_j q_j' \right) (h_i(t) - h_b(t)) + \sum_j q_j^0 + r_i}{\frac{S_i}{\delta t} + T_i - \sum_j q_j'}, \tag{42}$$

$$q_i' = -T_i \frac{\frac{S_i}{\delta t} - \sum_j q_j'}{\frac{S_i}{\delta t} + T_i - \sum_j q_j'}. \tag{43}$$

300 Thus, q_i^0 and q_i' can be computed successively in downstream order, starting from the nodes without donors.

However, $q_i(t + \delta t)$ cannot be computed during the downstream sweep since the actual values $h_b(t + \delta t)$ required in Eq. (41) are still unknown. Computing the values $h_i(t + \delta t)$ and $q_i(t + \delta t)$ requires a second sweep over all nodes, which has to be performed in opposite direction (upstream, starting from the boundary). As soon as $h_b(t + \delta t)$ is known (since the node b is treated prior to the node i), $q_i(t + \delta t)$ can be computed from Eq. (41). Finally, the hydraulic head can be calculated from

305 Eq. (14) according to

$$h_i(t + \delta t) = h_b(t + \delta t) + \frac{q_i(t + \delta t)}{T_i}. \tag{44}$$

This scheme provides a direct solver (without the need for iterations) for the fully implicit discretization of the flow equation on a dendritic network. It is therefore stable for arbitrary time increments δt, and its performance is not affected by spatial variations in transmissivity and storativity. The numerical complexity is $O(n)$, which means the the computing effort increases

310 only linearly with the total number of nodes. It is therefore perfectly suited for simulations on grids with several millions of nodes.

2.6   Nondimensionalization

The linearized problem (Eq. 7, where T does not depend on h) can easily be transformed to nondimensional properties, which makes the results independent of the absolute values of S and T and of the spatial scale. For this purpose, arbitrary reference

values S_0 and T_0 and an arbitrary length scale l can be defined. Then the respective nondimensional properties

$$\hat{S} = \frac{S}{S_0}, \quad \hat{T} = \frac{T}{T_0}, \quad \text{and} \quad \hat{x} = \frac{x}{l} \tag{45}$$

are defined. If we further introduce

$$t_0 = \frac{S_0 l^2}{T_0} \quad \text{and} \quad r_0 = \frac{T_0}{l} \tag{46}$$

and define the nondimensional properties

$$\hat{h} = \frac{h}{l}, \quad \hat{t} = \frac{t}{t_0}, \quad \text{and} \quad \hat{r} = \frac{r}{r_0}, \tag{47}$$

the differential equation for the nondimensional properties is the same as the original equation (Eq. 7). This result can easily be verified by expressing the original properties in Eq. (7) in terms of the respective nondimensional properties. The scaling factor for the flux density is T_0 then, so $\boldsymbol{q} = T_0 \hat{\boldsymbol{q}}$.

As a consequence of these scaling properties, the shape of the instantaneous unit hydrograph depends only on the shape of the aquifer and on the spatial pattern of S and T, but not on their absolute values and on the absolute size of the aquifer. This property will turn out to be useful in the following section.

2.7 Patterns of transmissivity and storativity

While systematic knowledge about the spatial structure of preferential flow paths is still limited, we need a model for generating spatial patterns of transmissivity and storativity. In this study, we adopt the theory based on minimum energy dissipation proposed by Hergarten et al. (2014). This theory addresses the best spatial distribution of a given total pore space volume in the sense that the total energy dissipation of steady-state flow is minimized. The central assumption behind this theory is a power-law relation between the hydraulic conductivity K on the porosity ϕ,

$$K \propto \phi^n, \tag{48}$$

with a given exponent n. Some ideas how dissolution could increase K were discussed in that study. If all pores have the same diameter and grow uniformly, an exponent $n = 2$ was obtained. The same result was obtained for an arbitrary distribution diameters if all pores grow by the same factor in diameter. In turn, a stronger increase in K with ϕ ($n > 2$) occurs if dissolution mainly affects the largest pores. Overall, these simple models yield a weaker increase in conductivity with porosity than predicted by the fundamental relation of Kozeny (1927) and Carman (1937). This relation predicts $n = 3$ at small porosities, which was also adopted in the numerical study of dissolution and precipitation by Edery et al. (2021). In turn, the theoretical study of fractal pore spaces by Costa (2006) points towards $n \approx 2$.

The exact value of the exponent n is, however, not important in the following. Theoretically, it is only important that the increase in K with ϕ is stronger than linear ($n > 1$) since concentrating porosity along preferential flow structures is energetically favorable only under this condition.

Based on the power-law relation, Hergarten et al. (2014) derived the relations

$$\phi \propto q^{\frac{2}{n+1}}, \tag{49}$$

$$K \propto q^{\frac{2n}{n+1}}. \tag{50}$$

and computed optimized dendritic networks on a discrete grid. This result is, however, limited to confined aquifers with a constant thickness. Assuming $S = \phi$ for an unconfined aquifer is the simplest and somehow straightforward approach. In turn, the transfer from K to T is not trivial and depends on the topography of the base b. Even if the bottom is flat, points with the same q will have different values of h and thus different $T = K(h - b)$, depending on their position in the network. Since this dependency would make the theory of minimum energy dissipation more complicated, it is assumed in the following that the dependence of T on q is the same as that of K (Eq. 50). As a modification, we might take into account that sites with high q and thus high K may have a lower thickness $h - b$. Then the increase in T with ϕ will be weaker than the increase in K, which could be included by reducing the exponent n.

As the most important aspect, however, Eqs. (49) and (50) refer to a steady state. The aquifer's properties do not change on the time scale of individual events. Instead, we assume that S and T are adjusted to a steady state that reflects some long-term average. At this point, we can make use of the nondimensional formulation developed in Sect. 2.6. Single-pixel catchments (nodes without donors) have the lowest values of S and T. Let us use their storativity and transmissivity as the reference values S_0 and T_0. If we assume a uniform long-term average recharge, the mean flux is proportional to the catchment size A_i of the respective node. If we further use the grid spacing d as the characteristic length scale l, the nondimensional generalization of Eqs. (49) and (50) is

$$S_i = A_i^{\frac{2}{n+1}}, \tag{51}$$

$$T_i = A_i^{\frac{2n}{n+1}}. \tag{52}$$

Owing to the choice $l = d$, the catchment size A_i has to be measured in grid pixels (so in units of d^2) here. Then single-pixel catchments are characterized by $S_i = T_i = 1$, corresponding to $S_i = S_0$ and $T_i = T_0$ in physical units.

The largest catchments in the examples considered later consist of slightly more than 10^6 pixels, which means that the catchment size varies by a bit more than six orders of magnitude. For $n = 2$, this corresponds to a variation in T by eight orders of magnitude. If we assume, e.g., $T_0 = 10^{-9}$ m^{2}s^{-1}, the values of T would cover the range from fresh limestone to strongly karstified limestone at a thickness of some meters. The respective range of S is only slightly more than four orders of magnitude for $n = 2$. However, assuming $S_0 = 10^{-5}$ would cover the range up to $S = 0.1$.

Practically, the characteristic timescale t_0 (Eq. 46) is the central property to be taken into account when transferring nondimensional hydrographs to real-world coordinates. With the values S_0 and T_0 defined above, this time scale would be $t_0 = 10^4$ s at a grid spacing $d = 1$ m and $t_0 = 10^6$ s at $d = 10$ m. Since d seems to be a numerical parameter rather than a physical parameter, the strong dependence on d may be confusing at first. However, d is a property of the spatial pattern. It defines the smallest cell that cannot be subdivided by a preferential flow pattern and thus some kind of representative elementary volume (in combination with the thickness).
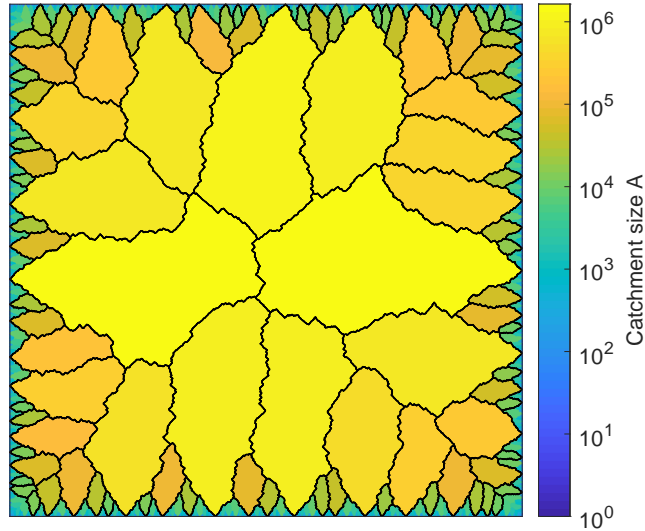
Figure 1. Catchments of numerically obtained dendritic flow patterns for $n = 2$ on a lattice of 4096×4096 sites. Color corresponds to the size A of each individual catchment, measured in grid pixels. The watersheds between large catchments ($A \geq 10000$ pixels) are highlighted in black.

The characteristic timescale t_0 can be interpreted physically in the setup used here. According to Eqs. (14) and (15), the smallest spatial unit (a single-pixel catchment) is described by the equation

$$d^2 S_0 \frac{\partial h_i}{\partial t} = -T_0 \left(h_i - h_b \right) \tag{53}$$

380 for zero recharge. So the smallest spatial units behave like a linear reservoir with a recession coefficient

$$\alpha = \frac{T_0}{d^2 S_0} = \frac{1}{t_0}, \tag{54}$$

which means that t_0 is the characteristic time of a single-pixel catchment.

2.8 Considered scenarios

Based on the assumptions described in the previous section, a numerically obtained flow pattern for $n = 2$ on a 4096×4096
385 grid is used in this study. The algorithm for generating such patterns was described by Hergarten et al. (2014). All points at the boundaries are considered as springs where the discharge is measured. Figure 1 illustrates the catchments of the springs.

Several scenarios will be considered for the same geometry in the following. Beside the reference scenario with $n = 2$, the influence of n will be investigated. These investigations also include uniform transmissivity and storativity. The suitability of the description as a dendritic network will be tested against full Darcy flow.

390 In order to enable a comparison of the recession curves of individual springs, the same catchments are used in all simulations. This means that the boundaries between the catchments shown in Fig. 1 are enforced by cutting the respective connections, so by inhibiting flow across the watersheds.
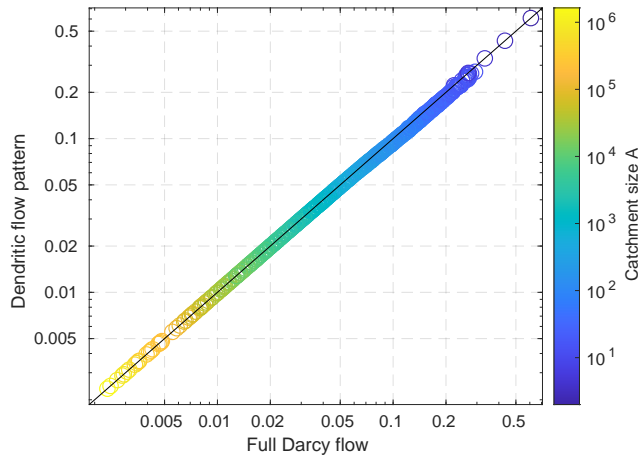
Figure 2. Recession coefficient α of each individual catchment with $n = 2$ for dendritic flow patterns against full Darcy flow. The colors match Fig. 1 and indicate the size of the respective catchment.

3 Results and discussion

3.1 Dendritic flow patterns vs. full Darcy flow

395 As a first step, we investigate under which conditions the reduction from full Darcy flow (taking all four neighbors into account) to a dendritic flow pattern (a single flow target for each node) provides a suitable approximation. We start from the optimized distribution of S and T for $n = 2$, so from a strongly preferential flow pattern. Figure 2 compares the long-term recession coefficients α (α_1 in Eq. 27) obtained from the dendritic flow pattern to those of full Darcy flow. The recession coefficients of both approaches agree well, which means that the long-term recession behavior is captured well by the dendritic flow pattern.

400 Some deviations occur at rather small catchment sizes from about 10 to 200. Here, allowing only one single flow direction leads to a slight underestimation of α, which means that the recession is slightly too slow. This underestimation is highest at catchment sizes $A \approx 16$ and reaches about 10 % there.

In order to investigate the effect of the restricted flow directions in more detail, we analyzed the flow pattern of the full Darcy scenario. For this purpose, we define the major flux component of each node as the flux towards the given flow target

405 (according to the dendritic pattern) and the minor flux component as the sum of the fluxes towards all other neighbors with lower head values.

Figure 3 shows the relative contribution of the minor fluxes as a function of the size of the respective upstream catchment. The upstream catchment size refers to the individual pixels here and not to the embedding catchment. So the data point for a $A = 1$ describes the average over all pixels without donors, no matter whether they are draining directly to the boundary (so

410 are indeed single-pixel catchments) or are part of a larger catchment. Since points at drainage divides are already restricted concerning their flow direction in the full Darcy scenario, these points are analyzed separately from inner points.
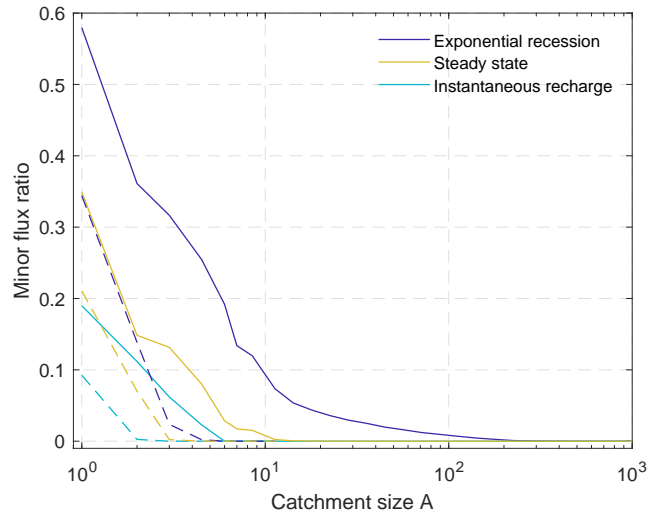
Figure 3. Relative contribution of the minor fluxes for each grid pixel as a function of the catchment size A. The curves were obtained by logarithmic binning with ten bins per decade. All three considered scenarios – a steady-state initial condition, a unit recharge pulse, and the exponentially decaying term (only the slowest component, first term in Eq. 27) – are analyzed separately for grid pixels that lie within a spring catchment (flow towards all four neighbors; solid lines) and pixels at drainage divides (restricted flow directions; dashed lines).

The contribution of the minor fluxes decreases with increasing catchment size, so downstream along the preferential flow paths. It becomes negligible for all considered scenarios at catchment sizes $A \gtrsim 200$. The contribution of the minor flux is particularly small immediately after a short, uniform recharge pulse. If all sites receive the same amount of water, the resulting change in hydraulic head is inversely proportional to the storativity. Since high transmissivity goes along with high storativity, the hydraulic gradient becomes more focused towards increasing catchment size. As a consequence, the fluxes are focused towards the preferential flow paths, which reduces the minor fluxes.

The strongest contribution of the minor fluxes is found for the long-term recession, characterized by an exponential recession curve. The minor fluxes contribute even almost 60 % for $A = 1$ here (only inner points, about 35 % for drainage divides). It may be surprising that the minor fluxes do not affect the recession coefficient strongly, as shown in Fig. 2. In an extreme scenario where all four neighbors are at the same head values, the fluxes would be four times higher in the full Darcy model than in the single flow target realization, which would result in a four times faster recession than predicted by Eq. 54. Although the majority of the nodes have small upstream catchment sizes (e.g., $A = 1$ for 43 % of all nodes and $A \leq 10$ for 81 % of all nodes), their behavior is obviously not crucial for the properties of the entire catchment.

These results suggest preferential flow patterns can be represented well on a discrete grid by a dendritic structure where each node drains only towards one of its neighbors. In turn, the approximation by a dendritic flow pattern does not work well for a spatially uniform distribution of T and S as shown in Fig. 4. Here, α is underestimated by more than one order of magnitude for large catchments, which means that the recession is more than by a factor of 10 too slow. The coefficients agree well only for small catchments, where the minor fluxes are small or even absent due to the restricted flow directions at drainage divides.
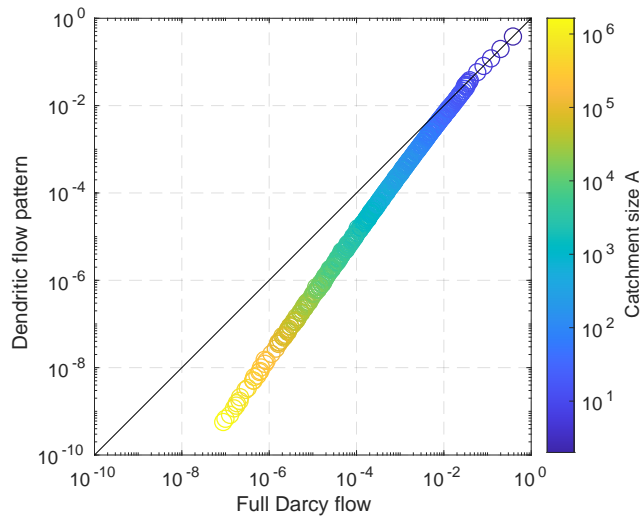
Figure 4. Recession coefficient α of each individual catchment with a spatially uniform distribution of T and S for dendritic flow patterns against full Darcy flow. The colors match Fig. 1 and indicate the size of the respective catchment.

3.2 Scaling properties of the recession coefficient

It was already visible in Figs. 2 and 4 that the recession coefficient α decreases with increasing catchment size. The expected scaling behavior is $\alpha \propto A^{-1}$. This result is formally obtained from the characteristic timescale t_0 (Eq. 46 with $A \propto l^2$), but can also be derived directly from the occurrence of a first-order time derivative at the left-hand side of Eq. (7) and second-order spatial derivatives at the right-hand side. If we rescale the entire catchment including the pattern of S and T by a factor β, the right-hand side of Eq. (7) changes by a factor of β^{-2} for $r = 0$. Then the time scale must change by the same factor. Since the catchment size A increases quadratically with β, the time scale is proportional to the catchment size and thus $\alpha \propto A^{-1}$.

As shown in Fig. 5, this simple scaling behavior does not hold for the patterns of S and T considered here. While the scaling behavior follows a power law

$$\alpha \propto A^{-\gamma} \tag{55}$$

reasonably well for all considered values of n, it seems that an exponent $\gamma = 1$ is only achieved for $n = 1$. For all values $n > 1$, we find $\gamma < 1$, where γ decreases with increasing n. This means that the recession of large catchments is still slower than the recession of small catchments, but the effect is considerably weaker than for a simple Darcy-type aquifer ($\gamma = 1$).

Qualitatively, this weaker increase is the expected behavior for a preferential flow pattern. Preferential flow paths are able to transport water rapidly over large distances, so that an increasing spatial extension does not slow down the recession as strongly as in a homogeneous aquifer.

The opposite behavior is observed for $n < 1$. Here large catchments become extremely slow. Revisiting Eqs. (51) and (52), it is recognized that T still increases with catchment size, but weaker than S for $n < 1$. So flow is still facilitated along the
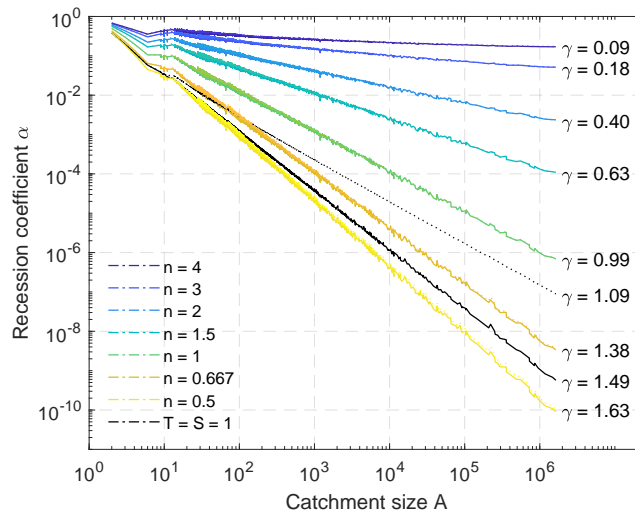
Figure 5. Scaling behavior of recession coefficient α relating to catchment size A (Eq. 55) for different values of n and for a uniform distribution of T and S. Full Darcy flow is plotted as solid lines, flow in dendritic patterns as dotted lines. Except for the scenario with $S = T = 1$, the curves of full Darcy flow and the dendritic pattern are hardly distinguishable.

preferential flow paths, but the respective cells become slow due to their high storativity. This becomes visible if we apply Eq. (54) formally to such cells, which yields $\alpha \propto A^{\frac{2(n-1)}{n+1}}$, so that α decreases with increasing A. However, $n < 1$ would be unrealistic for porous media, where rather $n \geq 2$ should be expected. Beyond this, it was demonstrated by Hergarten et al. (2014) that dendritic flow patterns are energetically favorable only for $n > 1$. So preferential flow patterns with $n < 1$ can be constructed, but do not make much sense. Nevertheless, the curves are almost indistinguishable not only for $n \geq 1$, but also for $n < 1$. The results reveal that the numerical approximation by a dendritic flow pattern also works well for $n < 1$.

As already recognized in Sect. 3.1, the approximation by a dendritic flow pattern does not work for constant transmissivity and storativity. Figure 5 reveals that the unusual scaling behavior with $\gamma > 1$ also occurs for the description by full Darcy flow. This result is related to the subdivision of the domain into fixed catchments drained by distinct springs. In order to test this hypothesis, we computed the recession coefficients for radial flow towards a spring in polar coordinates. Keeping the radius of the spring constant and varying the total size of the catchment (the outer radius), we obtained roughly the same scaling behavior, $\gamma \approx 1.1$, as found for the catchments considered in Fig. 5. This scaling behavior indicates that the region around the spring is some kind of bottleneck that becomes increasingly relevant for large catchments. This result aligns well with the result of Hergarten et al. (2014), who found that minimum energy dissipation for radial flow requires an increase in permeability towards the spring.

The nontrivial dependence of α on the catchment size does not only affect spring hydrographs, but also the response time of aquifers to changes in climate or hydraulic conditions at the boundaries. As a recent example, Cuthbert et al. (2019) provided worldwide estimates of these groundwater response times worldwide. These estimates are based on the one-dimensional version of Eq. (7) for homogeneous aquifers with the size of the aquifer assumed to be twice the distance L of perennial rivers.
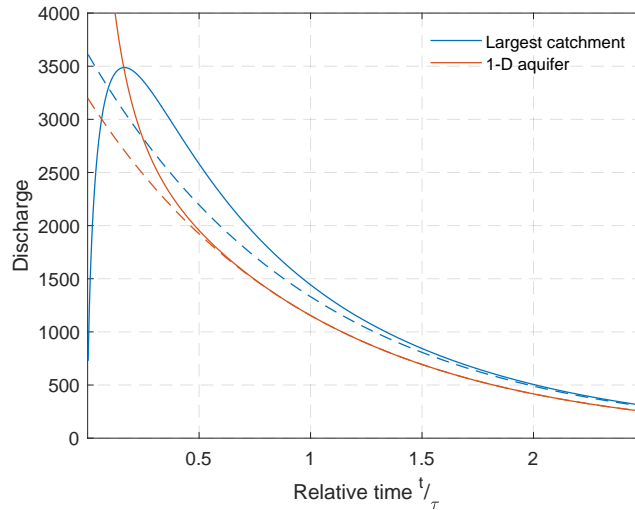
Figure 6. Unit hydrographs of the biggest catchment for $n = 2$ and of a homogeneous 1-D aquifer. The dashed lines correspond to the long-term exponential recession. The data are scaled in such a way that the e-folding time τ and the total amount of water supplied by the recharge event are the same in both scenarios.

Then the scaling arguments given above (and formally in Sect. 2.6) yields $\alpha \propto L^{-2}$ and thus a response time proportional to L^2. Since L increases with decreasing precipitation, this model predicts a strong negative correlation between precipitation and groundwater response time with typical response times of several thousand years in arid and semi-arid regions. If the respective aquifers are not homogeneous, but have a preferential flow structure as considered here, the dependence of the groundwater response time on L and thus on climate will be considerably weaker than predicted by Cuthbert et al. (2019).

3.3 Short-term recession

The differences between the model considered here and simple Darcy-type models are not limited to the scaling properties of the long-term recession coefficient. As exemplified in Fig. 6 for the biggest catchment, the unit hydrograph shows a clear rising limb at short times. In contrast, the 1-D Darcy-type aquifer shows a power-law decrease in discharge at short times, so that $Q \to \infty$ for $t \to 0$.

For a better comparison, size and parameter values of the 1-D aquifer were adjusted in such a way that the long-term recession coefficient α and the total amount of water supplied by the recharge event are the same as for the considered catchment (see Appendix B). For such a simple aquifer, a lag between a short precipitation event and the peak discharge would typically be attributed to the infiltration process. We would then assume that the time lag is related to the transit time of the water from the surface to the aquifer. In a model consisting of individual porous blocks connected by highly conductive fractures (e.g., Kovács et al., 2005; Hergarten and Birk, 2007), the time lag may also be owing to the finite conductivity of the fracture system. In contrast, the finite rise time is an inherent property of the structure of the aquifer in the model considered here. It cannot be attributed uniquely to any individual component of the system.
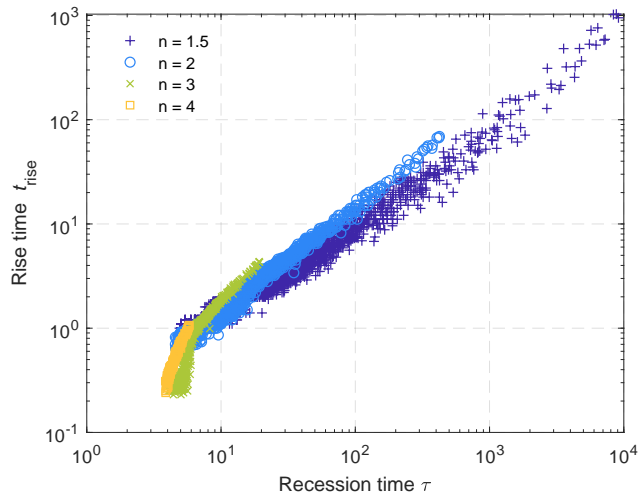
Figure 7. Relation between rise time t_{rise} and e-folding time τ of the long-term recession for the considered catchments and different values of n.

485   Figure 7 provides an analysis of the rise time t_{rise} for the considered catchments and different values of the exponent n. For $n = 2$, the data suggest a linear relationship between t_{rise} and the long-term e-folding time $\tau = \frac{1}{\alpha}$. The ratio of t_{rise} and τ varies from about 9 % to 19 % for the individual catchments. The rise times become slightly shorter in relation to the e-folding time for lower n. For $n = 1.5$, we found ratios in a range from about 4 % to 22 %. The data obtained for $n > 2$ are non-unique, in particular for small catchments (small τ). Overall, there seems to be a weak increase in the ratio of t_{rise} and τ with increasing

490   n. This trend aligns well with the absence of a finite rise time in the simple one- and two-dimensional aquifers without a preferential flow pattern. However, the trend is much weaker than the variation among individual catchments and therefore not investigated further. In each case, however, t_{rise} is not very small compared to τ. One-seventh of the e-folding recession time seems to be a reasonable order of magnitude. Taking into account that long-term e-folding times of karst aquifers are typically in an order of magnitude of several weeks, the rise time is in an order of magnitude of several days.

495   The occurrence of a rising limb in the unit hydrograph requires that some of the coefficients $\lambda_k Q_k$ in Eq. (27) are negative. This can be seen formally by computing the derivative of Eq. (27). The derivatitve is similar to Eq. (27) itself, except that the coefficients are $-\alpha_k \lambda_k Q_k$. Since the sum cannot become zero if all coefficients have the same sign, at least one of the original coefficients $\lambda_k Q_k$ must be negative. Figure 8 shows the coefficients for the largest catchment. While the coefficients of the slowest components (small α_k) are positive, there is no obvious preference for either sign in the faster components.

500   The spectrum of the considered catchment differs fundamentally from that of the 1-D aquifer. While the spectrum of the 1-D aquifer consists of distinct components with recession coefficients $\alpha_k \propto (2k-1)^2$ (see Appendix B), the spectrum of the catchment becomes more or less continuous at large k. However, the smallest recession coefficients are still distinct. For the catchment analyzed in Fig. 8, the ratio is $\frac{\alpha_2}{\alpha_1} \approx 2$. While the lowest ratios among all simulated catchments are about 1.5, the ratio is typically in a range from about 2.5 to 4 for smaller catchments. So the ratio $\frac{\alpha_2}{\alpha_1}$ differs from catchment to catchment,
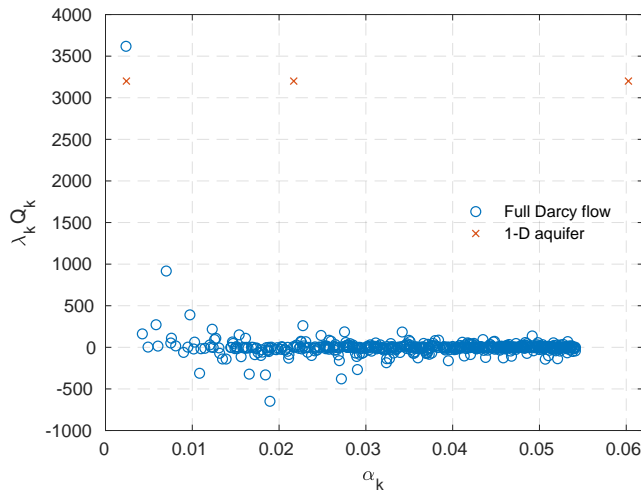
Figure 8. Coefficients $\lambda_k Q_k$ and recession coefficients α_k in Eq. (27) for the largest catchment ($n = 2$). Only the slowest 500 components ($k \leq 500$) were computed. The data of the 1-D aquifer were rescaled in such a way that the lowest recession coefficient α_1 and the total recharge are the same as for the simulated catchment.

505 but is always clearly above unity. This also holds for $n \neq 2$. This property ensures that the recession curve approaches a single exponential function at a reasonable time and that the coefficient $\lambda_1 Q_1$ captures the long-term recession well. However, the ratio is much lower than the ratio $\frac{\alpha_2}{\alpha_1} = 9$ of the 1-D aquifer. Although the deviation from an exponential recession also depends on the coefficients $\lambda_k Q_k$, the difference is already visible in Fig. 6. While the unit hydrograph of the 1-D aquifer is almost indistinguishable from the exponential decay at $t = 0.5\tau$, the difference is more than 15 % at this time for the largest

510 catchment. So the model with the preferential flow pattern approaches the long-term exponential recession much more slowly than the simple 1-D aquifer.

Figure 9 illustrates the approximation of the unit hydrograph by a finite number of exponential components. In this example, all coefficients for $k \leq 9$ are positive. In the range $9 < k \leq 23$, there are also negative coefficients. However, the positive coefficients still dominate here, so that the highest peak discharge is achieved when including the components with $k \leq 23$.

515 The negative components become increasingly relevant for larger k. This results in a decreasing peak discharge, however, still at $t = 0$ for $k \leq 60$. The component with $k = 61$ is the first that shifts the peak discharge to a time $t > 0$ an thus produces a rising limb in the unit hydrograph. However, approximating the behavior around the peak discharge reasonably well requires several hundred components.

The occurrence of negative coefficients in Eq. (27) is not a fundamental problem, but impedes a simple interpretation of the

520 decomposition into exponentially decreasing terms. If all components were positive, we could imagine the aquifer as a set of linear reservoirs drained in parallel. However, negative components would correspond to reservoirs with a negative amount of water. Formally, the slow component (first exponential function) could even contain more water than available in total, and the fast components (all higher exponentials) could be negative in total. In Fig. 6, this would mean that the area of the unit
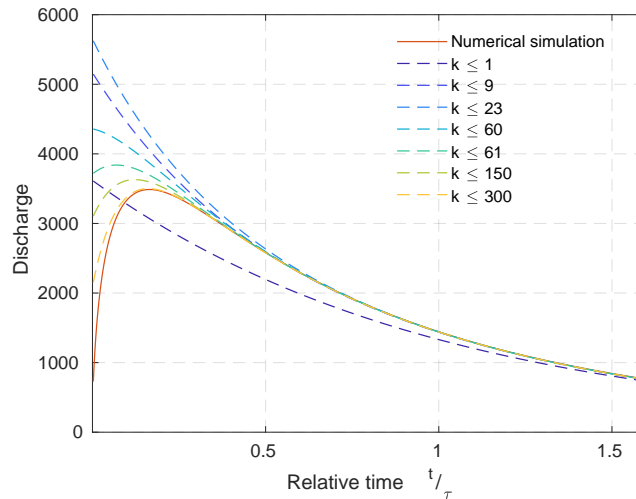
Figure 9. Recession curves of the largest catchment obtained from the numerical simulation and different numbers of exponential functions (Eq. 27).

hydrograph below the exponential component at short times was larger than the area above the exponential component. In this
525   case, the widely used characterization of karst aquifers by the contribution of the slow (exponential) component to the total discharge (Mangin, 1975; Jeannin and Sauter, 1998) would be taken at absurdum.

Figure 10 shows the contribution of the slow component (first exponential) to the total amount of water for all catchments considered here ($n = 2$). Depending on the catchment size, this contribution is between 77 % and 104 %. So there are indeed catchments where the effect of the rising limb is so strong that the slow component is formally larger than the total recharge
530   and the fast components are negative in sum. However, this effect is found only for some rather small catchments. For the largest catchments, the contribution of the slow component is about 90 %.

The obtained contributions of the slow component are high compared to other models. For the 1-D aquifer used here as a reference, this contribution is $\frac{8}{\pi^2} \approx 81$ %. For an aquifer consisting of square porous blocks connected by conduits with infinite conductance, it is $\frac{64}{\pi^4} \approx 66$ % (e.g., Birk and Hergarten, 2010). The contribution of the slow component was not explicitly
535   investigated by Hergarten and Birk (2007) in their fractal model with power-law distributed block sizes. However, since the slowest flow component arises from the largest blocks, the total contribution of the slow component must even be considerably smaller than the 66 % obtained for an aquifer with a uniform block size. In the widely used classification scheme of karst aquifers proposed by Mangin (1975), even aquifers with a contribution of the slow component of less than 50 % are considered poorly karstified (see also Jeannin and Sauter, 1998). So our continuous model of preferential flow patterns predicts even a
540   higher contribution of the slow component to the unit hydrograph than other models and is far off from what is typically assumed for karst systems.

At first sight, the observed high contribution of the slow component could be an effect of the finite rise time. As recognized in Figs. 6 and 9, the unit hydrograph is below the slow component for $t \lesssim 0.5 t_{\mathrm{rise}}$. When investigating recession curves in reality,
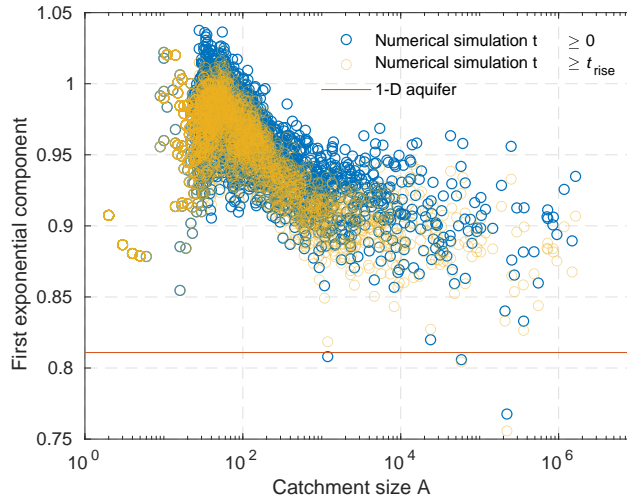
Figure 10. Contribution of the slowest exponential component to the total discharge for the considered catchments. The red line shows the respective contribution of $\frac{8}{\pi^2} \approx 81\ \%$ for the 1-D aquifer.

the analysis typically starts from the peak in discharge ($t = t_{\mathrm{rise}}$). The orange-colored markers in Fig. 10 show the respective
545   contributions of the slow component. Starting the analysis from $t = t_{\mathrm{rise}}$ instead of $t = 0$ indeed yields lower contributions of the slow components. However, the effect is only in an order of magnitude of a few percent. So the result that continuous preferential flow patterns predict a high contribution of the slowest flow component is not an artifact of the analysis.

3.4   The effect of non-uniform recharge

While the unit hydrograph describes uniform recharge, the spatial distribution of the recharge may have a strong influence on
550   recession curves of large catchments. So the question arises whether the strong deviations from the exponential behavior found for karst springs could be related to the occurrence of local rainstorms that affect only a small part of the catchment.

As a simple example, we separated the domain into a proximal part and a distal part. Both parts are equally sized, and the distinction is made by the distance from the boundary of the domain. Since the overall domain is the same, the recession coefficients α_k of all flow components are the same as for the entire domain. Only the coefficients a_k in Eq. (27) differ. This
555   difference, however, has a strong effect on the rise time and on the contribution of the slow flow component.

Figure 11 compares the results obtained numerically for the largest catchment to those obtained by spectral decomposition for a 1-D aquifer (for details, see Appendix B). While the hydrograph starts with a peak at $t = 0$ after a spatially uniform recharge event, applying recharge only to the distal part of the domain introduces a finite rise time. This rise time is, however, shorter (in relation to the e-folding recession time) than for the aquifer with the preferential flow pattern. The rise time of the
560   preferential flow pattern also changes considerably if recharge is applied only to a part of the domain. The strong influence may be surprising at first since we could expect that the signal propagates rapidly through the preferential flow structure from
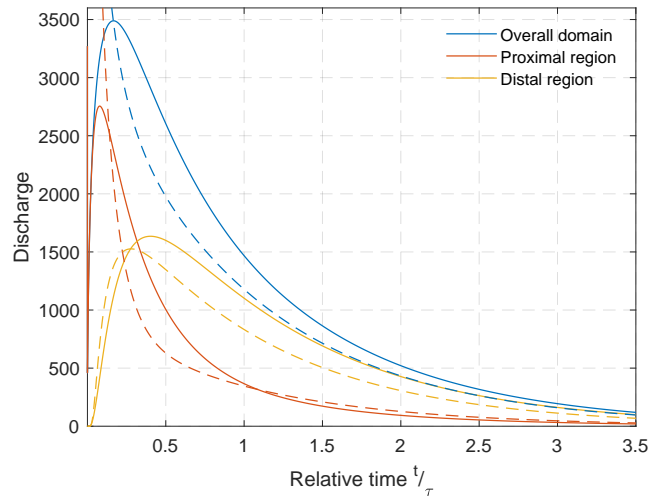
Figure 11. Instantaneous unit hydrographs for recharge applied to a part of the domain. Solid lines refer to the largest catchment of the simulation, and dashed lines to a homogeneous aquifer. The data are scaled in such a way that the e-folding time τ and the total amount of supplied water are the same in both scenarios. Proximal and distal regions cover half of the catchment each.

the distal part of the domain to the spring. However, preferential flow paths have not only a high transmissivity here, but also a high storativity. Thus, the propagation of signals is not as fast as we might expect.

The contribution of the slowest component also changes if recharge is applied only to a part of the domain. Similarly to the
565   rise time, it increases if only the distal part of the domain is filled since the instantaneous recharge signal has already been smoothed when it arrives at the spring. The contribution of the first exponential component is formally higher than 100 % for the distal part. For the largest simulated catchment, it is 137 %, while it is 115 % for the 1-D aquifer. In turn, the contribution of the first exponential component is lower for the proximal parts; 50 % for the largest catchment in the simulation and 47 % for the 1-D aquifer. So the contribution of the first exponential component is always higher for the preferential flow pattern than
570   for the 1-D aquifer, and the effect of applying recharge only to a part of the domain is similar.

On average, however, the effect vanishes. For the largest catchment, the 50 % for the proximal region and the 137 % for the distal region yield a mean value of 94 % in agreement with Fig. 10 (rightmost blue circle). This is a general property of the linear model, which allows for superposing recharge events not only concerning time, but also spatially. It could even be generalized to arbitrary parts of the domain down to recharge events that are limited to a single node.
575   While there should theoretically be no effect on average, recharge events in the proximal region will be more prominent in the hydrograph than those in the distal region. Therefore, the analysis of real-world hydrographs might be biased towards the more prominent, proximal recharge events, which would yield a decreasing contribution of the slowest component for large catchments. However, explaining the often small contribution of the exponential component this way seems quite a stretch.

4 Conclusions and perspectives

580 This study is a first attempt to describe the dynamics of aquifers with continuous preferential flow patterns. In contrast to approaches based on two or three distinct flow components widely used in the context of karst aquifers, the concept used here assumes a continuous spatial variation in hydraulic properties over several orders of magnitude.

A two-dimensional aquifer with a spatially variable, but time-independent transmissivity was considered. This scenario corresponds to the application of small disturbances to a steady state of an aquifer with an almost horizontal water table. 585 Synthetic spatial patterns of transmissivity and storativity were obtained from principles of minimum energy dissipation based on the theory proposed by Hergarten et al. (2014).

As a major technical result, it was found that such aquifers can be approximated well by dendritic flow patterns, in which the entire discharge of each cell is delivered to the neighbor with the steepest gradient in hydraulic head. This approximation has been widely used for channelized flow patterns at the surface. The dendritic structure enables an efficient, fully implicit 590 numerical scheme with a numerical effort that increases only linearly with the number of cells, also known as $O(n)$ complexity. This property allows for simulations on grids consisting of several million nodes and thus for a reasonable spatial resolution of the preferential flow pattern.

As a second, rather theoretical result, it was shown that spectral theory is not restricted to homogeneous aquifers, but can also be applied to aquifers with any spatial distribution of transmissivity and storativity. Although the eigenvalues and the 595 respective eigenvectors have to be computed numerically, this approach allows for a fast computation of the long-term recession coefficient without forward modeling over a long time span. In addition, the contribution of the slowest flow component to the instantaneous unit hydrograph (and also to any other initial state) can be computed easily. However, the efficient numerical scheme and spectral theory rely on the assumption of time-independent transmissivity and cannot be extended easily towards sloping aquifers.

600 The long-term recession coefficient α depends on the catchment size. The dependency is, however, weaker than for homogeneous aquifers and follows a power law $\alpha \propto A^{-\gamma}$ (Eq. 55). The exponent γ depends on the assumed relation between transmissivity T and storativity S. It approaches 1 for $T \propto S$, which is also the limit where dendritic flow patterns are energetically favorable. In this case, the scaling is the same as for homogeneous aquifers ($\gamma = 1$). For relations $T \propto S^n$, γ decreases with increasing n. As a typical value, $\gamma = 0.4$ was found for $n = 2$. So the decrease in the recession coefficient with catchment 605 size is typically less than half as strong as for homogeneous aquifers. This finding challenges previous results on very long groundwater response times of large aquifers (e.g., Cuthbert et al., 2019).

Since flow patterns obtained from minimum energy dissipation are typically scale-invariant, a power-law decrease of the discharge after a short recharge pulse might be expected at first. However, the respective instantaneous unit hydrograph shows a completely different behavior. The discharge immediately after the recharge event is quite small, and it takes a considerable 610 time until it reaches its peak. This rise time is in an order of magnitude of one-seventh of the e-folding recession time ($\tau = \alpha^{-1}$). It seems neither to depend strongly on the catchment size nor on the relation between transmissivity and storativity.

The contribution of the slowest component to the unit hydrograph is in an order of magnitude of 90 % for large catchments and even larger for small catchments. This contribution increases further if recharge is applied only to a part of the domain far away from the spring and even exceeds 100 % then. Formally, this result arises from the occurrence of negative coefficients in
615 decomposition of the unit hydrograph into exponentially decaying components. The occurrence of negative coefficients also inhibits the simple interpretation as a set of linear reservoirs draining in parallel. Measuring the contribution of the slowest component from the peak of the unit hydrograph instead of the time at which the instantaneous recharge occurs reduces the contribution of the slowest component only slightly. This contribution is higher than for homogeneous aquifers and much higher than typically assumed for karst aquifers (less than 50 %).

620 So we have to conclude that preferential flow patterns arising from a strongly organized pattern of transmissivity and storativity differ fundamentally from karst aquifers in their properties. For future work, it would be interesting to find out whether the difference mainly concerns the contribution of the slowest flow component or also the scaling of the recession coefficient with catchment size.

For the further development, an extension of the numerical scheme towards unconfined sloping aquifers (e.g., Rupp and
625 Selker, 2006; Pauritsch et al., 2015) would be particularly useful. Although there is ongoing development in this field (e.g., Alemie et al., 2019; Pathania et al., 2019), including preferential flow patterns at a reasonable spatial resolution is still a challenge here. Extending the implicit scheme for dendritic flow patterns towards unconfined sloping aquifer would still be challenging, but might considerably contribute to understanding the response of hillslopes to precipitation events and phenomena such as subsurface stormflow (e.g., Chifflard et al., 2019).

Appendix A: The fully implicit scheme for a dendritic network

In this section, Eqs. (42) and (43), which are the basis of the implicit scheme discussed in Sect. 2.5, are proven. Inserting Eqs. (14) and (41) into Eq. (40) yields

$$S_i \frac{h_i(t+\delta t) - h_i(t)}{\delta t} = -T_i \left(h_i(t+\delta t) - h_b(t+\delta t) \right) + \sum_{j \in D(i)} q_j^0 + \sum_{j \in D(i)} q_j' \left(h_i(t+\delta t) - h_i(t) \right) + r_i, \tag{A1}$$

and thus

635 $$h_i(t+\delta t) - h_i(t) = \frac{T_i \left(h_b(t+\delta t) - h_i(t) \right) + \sum_j q_j^0 + r_i}{\frac{S_i}{\delta t} + T_i - \sum_j q_j'}. \tag{A2}$$

Using Eq. (14), we can then compute the flux according to

$$q_i(t+\delta t) = T_i \left(h_i(t+\delta t) - h_b(t+\delta t) \right) \tag{A3}$$

$$= T_i \left(\frac{T_i \left(h_b(t+\delta t) - h_i(t) \right) + \sum_j q_j^0 + r_i}{\frac{S_i}{\delta t} + T_i - \sum_j q_j'} + h_i(t) - h_b(t+\delta t) \right) \tag{A4}$$

$$= T_i \frac{\left(\frac{S_i}{\delta t} - \sum_j q_j' \right) \left(h_i(t) - h_b(t+\delta t) \right) + \sum_j q_j^0 + r_i}{\frac{S_i}{\delta t} + T_i - \sum_j q_j'}. \tag{A5}$$

640 Then q_i^0 (Eq. 42) is obtained by setting $h_b(t+\delta t) = h_b(t)$ and and q_i' (Eq. 43) by taking the derivative with respect to $h_b(t+\delta t)$.

Appendix B: The unit hydrograph of a homogeneous 1-D aquifer

Let us consider a 1-D aquifer with a length L, where the spring is located at $x = 0$ and the drainage divide at $x = L$. Then the boundary conditions are $h(x,t) = 0$ at $x = 0$ and $\frac{\partial}{\partial x} h(x,t) = 0$ at $x = L$, and $h(x,t)$ is periodic with a wavelength of $4L$. Thus, $h(x,0)$ can be written as a Fourier series

$$h(x,0) = \sum_{k=1}^{\infty} a_k \sin\left(\frac{2\pi k x}{4L}\right),\tag{B1}$$

where the respective terms with the cosine function are zero due to the boundary conditions and $a_k = 0$ for even values of k. The coefficients a_k are given by the relation

$$a_k = \frac{2}{4L} \int_0^{4L} h(x,0) \sin\left(\frac{2\pi k x}{4L}\right) dx = \frac{2}{L} \int_0^{L} h(x,0) \sin\left(\frac{2\pi k x}{4L}\right) dx.\tag{B2}$$

If we assume that the distal region, $\lambda L \leq x \leq L$ with $\lambda \in [0,1]$, is initially filled to a given head value h_0, we obtain

$$a_k = \frac{2h_0}{L} \int_{\lambda L}^{L} \sin\left(\frac{2\pi k x}{4L}\right) dx = \frac{4h_0}{\pi k} \cos\left(\frac{\pi k \lambda}{2}\right)\tag{B3}$$

for uneven values of k. The time-dependent solution $h(x,t)$ must satisfy the 1-D version of Eq. (7) with $r = 0$,

$$S\frac{\partial h}{\partial t} = \frac{\partial}{\partial x}\left(T\frac{\partial h}{\partial x}\right).\tag{B4}$$

It is easily recognized that the solution of this equation with the initial condition defined by Eq. (B1) is

$$h(x,t) = \sum_{k=1}^{\infty} a_k \sin\left(\frac{2\pi k x}{4L}\right) e^{-\alpha_k t},\tag{B5}$$

where

$$\alpha_k = \frac{T}{S}\left(\frac{\pi k}{2L}\right)^2.\tag{B6}$$

Then the flux per unit width across the boundary is

$$q(t) = T\frac{\partial}{\partial x} h(x,t)\Big|_{x=0} = T\sum_{k=1}^{\infty} a_k \frac{2\pi k}{4L} e^{-\alpha_k t} = \frac{2Th_0}{L} \sum_{\substack{k=1 \\ (\text{uneven})}}^{\infty} \cos\left(\frac{\pi k \lambda}{2}\right) e^{-\alpha_k t}\tag{B7}$$

with the coefficients a_k from Eq. (B3). The respective expression for the proximal region, $0 \leq x \leq \lambda L$, is readily obtained by subtracting this expression from the same expression with $\lambda = 0$.

Code and data availability. All codes and simulated data are available in a Zenodo repository at https://doi.org/10.5281/zenodo.7050521 (Strüven and Hergarten, 2022). The authors are happy to assist interested readers in reproducing the results and performing subsequent research.

Author contributions. J.S. developed the numerical codes and analyzed the results. S.H. developed the theoretical framework. Both authors wrote the paper.

Competing interests. The authors declare that there is no conflict of interest.

Acknowledgements. The authors would like to thank Erwin Zehe and an anonymous reviewer for their constructive comments and Monica Riva for the editorial handling. This work was funded by the Deutsche Forschungsgemeinschaft (DFG, German Research Foundation) – 414728598.

665

References

Alemie, T. C., Tilahun, S. A., Ochoa-Tocachi, B. F., Schmitter, P., Buytaert, W., Parlange, J.-Y., and Steenhuis, T. S.: Predicting shallow groundwater tables for sloping highland aquifers, Water Resour. Res., 55, 11 088–11 100, https://doi.org/10.1029/2019WR025050, 2019.

Atkinson, T. C.: Diffuse flow and conduit flow in limestone terrain in the Mendip Hills, Sommerset (Great Britain), J. Hydrol., 35, 93–110, https://doi.org/10.1016/0022-1694(77)90079-8, 1977.

Banavar, J. R., Maritan, A., and Rinaldo, A.: Size and form in efficient transportation networks, Nature, 399, 130–132, https://doi.org/10.1038/20144, 1999.

Basha, H. A.: Flow recession equations for karst systems, Water Resour. Res., 56, e2020WR027 384, https://doi.org/10.1029/2020WR027384, 2020.

Bernatek-Jakiel, A. and Poesen, J.: Subsurface erosion by soil piping: significance and research needs, Earth Sci. Rev., 185, 1107–1128, https://doi.org/10.1016/j.earscirev.2018.08.006, 2018.

Birk, S. and Hergarten, S.: Early recession behaviour of spring hydrographs, J. Hydrol., 387, 24–32, https://doi.org/10.1016/j.jhydrol.2010.03.026, 2010.

Birk, S., Liedl, R., Sauter, M., and Teutsch, G.: Hydraulic boundary conditions as a controlling factor in karst genesis: A numerical modeling study on artesian conduit development in gypsum, Water Resour. Res., 39, 1004, https://doi.org/10.1029/2002WR001308, 2003.

Carman, P. C.: Fluid flow through granular beds, Trans. Inst. Chem. Engin. London, 15, 150–166, 1937.

Chifflard, P., Blume, T., Maerker, K., Hopp, L., van Meerveld, I., Graef, T., Gronz, O., Hartmann, A., Kohl, B., Martini, E., Reinhardt-Imjela, C., Reiss, M., Rinderer, M., and Achleitner, S.: How can we model subsurface stormflow at the catchment scale if we cannot measure it?, Hydrol. Process., 33, 1378–1385, https://doi.org/0.1002/hyp.13407, 2019.

Costa, A.: Permeability-porosity relationship: A reexamination of the Kozeny-Carman equation based on a fractal pore-space geometry assumption, Geophys. Res. Lett., 33, L02 318, https://doi.org/10.1029/2005GL025134, 2006.

Cuthbert, M. O., Gleeson, T., Moosdorf, N., Befus, K. M., Schneider, A., Hartmann, J., and Lehner, B.: Global patterns and dynamics of climate–groundwater interactions, Nature Clim. Change, 9, 137–141, https://doi.org/10.1038/s41558-018-0386-4, 2019.

de Rooij, G. H.: Is the groundwater reservoir linear? A mathematical analysis of two limiting cases, Hydrol. Earth Syst. Sci. Discuss., 11, 83–108, https://doi.org/10.5194/hessd-11-83-2014, 2014.

Drogue, C.: Analyse statistique des hydrogrammes de decrues des sources karstiques, J. Hydrol., 15, 49–68, https://doi.org/10.1016/0022-1694(72)90075-3, 1972.

Edery, Y., Stolar, M., Porta, G., and Guadagnini, A.: Feedback mechanisms between precipitation and dissolution reactions across randomly heterogeneous conductivity fields, Hydrol. Earth Syst. Sci., 25, 5905–5915, https://doi.org/10.5194/hess-25-5905-2021, 2021.

Enquist, B. J., Brown, J. H., and West, G. B.: Allometric scaling of plant energetics and population density, Nature, 395, 163–165, https://doi.org/10.1038/25977, 1998.

Enquist, B. J., West, G. B., Charnov, E. L., and Brown, J. H.: Allometric scaling of production and life-history variation in vascular plants, Nature, 401, 907–911, https://doi.org/10.1038/44819, 1999.

Fenicia, F., Savenije, H. H. G., Matgen, P., and Pfister, L.: Is the groundwater reservoir linear? Learning from data in hydrological modelling, Hydrol. Earth Syst. Sci., 10, 139–150, https://doi.org/10.5194/hess-10-139-2006, 2006.

Fiorillo, F.: The recession of spring hydrographs, focused on karst aquifers, Water Resour. Manage., 28, 1781–1805, https://doi.org/10.1007/s11269-014-0597-z, 2014.

Forkasiewicz, J. and Paloc, H.: Le régime de tarissement de la Foux-de-la-Vis. Etude préliminaire., Chron. hydrogéol., 3, 61–73, 1967.

Hackbusch, W.: Multi-Grid Methods and Applications, Springer, Berlin, Heidelberg, New York, https://doi.org/10.1007/978-3-662-02427-0, 1985.

710   Halmos, P.: Finite-Dimensional Vector Spaces, Springer, New York, 2nd edn., https://doi.org/10.1007/978-1-4612-6387-6, 1958.

Hergarten, S.: Transport-limited fluvial erosion – simple formulation and efficient numerical treatment, Earth Surf. Dynam., 8, 841–854, https://doi.org/10.5194/esurf-8-841-2020, 2020.

Hergarten, S. and Birk, S.: A fractal approach to the recession of spring hydrographs, Geophys. Res. Lett., 34, 11 401, https://doi.org/10.1029/2007GL030097, 2007.

715   Hergarten, S., Winkler, G., and Birk, S.: Transferring the concept of minimum energy dissipation from river networks to subsurface flow patterns, Hydrol. Earth Syst. Sci., 18, 4277–4288, https://doi.org/10.5194/hess-18-4277-2014, 2014.

Hergarten, S., Winkler, G., and Birk, S.: Scale invariance of subsurface flow patterns and its limitation, Water Resour. Res., 52, 3881–3887, https://doi.org/10.1002/2015WR017530, 2016.

Howard, A. D.: Theoretical model of optimal drainage networks, Water Resour. Res., 26, 2107–2117,
720   https://doi.org/10.1029/WR026i009p02107, 1990.

Jeannin, P.-Y. and Sauter, M.: Analysis of karst hydrodynamic behaviour using global approaches: a review, Bull. Hydrogeol., 16, 31–48, 1998.

Jeannin, P.-Y., Artigue, G., Butscher, C., Chang, Y., Charlier, J.-B., Duran, L., Gill, L., Hartmann, A., Johannet, A., Jourde, H., Kavousi, A., Liesch, T., Liu, Y., Lüthi, M., Malard, A., Mazzilli, N., Pardo-Igúzquiza, E., Thiéry, D., Reimann, T., Schuler,
725   P., Wöhling, T., and Wunsch, A.: Karst modelling challenge 1: Results of hydrological modelling, J. Hydrol., 600, 126 508, https://doi.org/10.1016/j.jhydrol.2021.126508, 2021.

Kaufmann, G. and Braun, J.: Karst aquifer evolution in fractured, porous rocks, Water Resour. Res., 36, 1381–1391, https://doi.org/10.1029/1999WR900356, 2000.

Kaufmann, G., Romanov, D., and Hiller, T.: Modeling three-dimensional karst aquifer evolution using different matrix-flow contributions, J.
730   Hydrol., 388, 241–250, https://doi.org/10.1016/j.jhydrol.2010.05.001, 2010.

Kleidon, A. and Renner, M.: Thermodynamic limits of hydrologic cycling within the Earth system: concepts, estimates and implications, Hydrol. Earth Syst. Sci., 17, 2873–2892, https://doi.org/10.5194/hess-17-2873-2013, 2013.

Kleidon, A. and Savenije, H. H. G.: Minimum dissipation of potential energy by groundwater outflow results in a simple linear catchment reservoir, Hydrol. Earth Syst. Sci. Discuss. (preprint), 2017, 1–11, https://doi.org/10.5194/hess-2017-674, 2017.

735   Kleidon, A. and Schymanski, S. J.: Thermodynamics and optimality of the water budget on land: a review, Geophys. Res. Lett., 35, L20 404, https://doi.org/10.1029/2008GL035393, 2008.

Kleidon, A., Renner, M., and Porada, P.: Estimates of the climatological land surface energy and water balance derived from maximum convective power, Hydrol. Earth Syst. Sci., 18, 2201–2218, https://doi.org/10.5194/hess-18-2201-2014, 2014.

Kleidon, A., Zehe, E., and Loritz, R.: ESD Ideas: Structures dominate the functioning of Earth systems, but their dynamics are not well
740   represented, Hydrol. Earth Syst. Sci. Discuss., https://doi.org/10.5194/esd-2019-52, 2019.

Kovács, A.: Quantitative classification of carbonate aquifers based on hydrodynamic behaviour, Hydrogeol. J., 29, 33–52, https://doi.org/10.1007/s10040-020-02285-w, 2021.

Kovács, A. and Perrochet, P.: A quantitative approach to spring hydrograph decomposition, J. Hydrol., 352, 16–29, https://doi.org/10.1016/j.jhydrol.2007.12.009, 2008.

745 Kovács, A. and Perrochet, P.: Well hydrograph analysis for the estimation of hydraulic and geometric parameters of karst and connected water systems, in: H2Karst Research in Limestone Hydrogeology, edited by Mudry, J., Zwahlen, F., Bertrand, C., and LaMoreaux, J., pp. 97–114, Springer, Cham, https://doi.org/10.1007/978-3-319-06139-9_7, 2014.

Kovács, A., Perrochet, P., Király, L., and Jeannin, P.-Y.: A quantitative method for the characterisation of karst aquifers based on spring hydrograph analysis, J. Hydrol., 303, 152–164, https://doi.org/10.1016/j.jhydrol.2004.08.023, 2005.

750 Kozeny, J.: Über kapillare Leitung des Wassers im Boden, Sitzungsber. Akad. Wiss. Wien, 136, 271–306, 1927.

Maillet, E.: Essais d'Hydraulique souterraine et fluviale, Librairie Scientifique A. Hermann, Paris, 1905.

Mangin, A.: Contribution a l'etude hydrodynamique des aquifères karstiques, Ph.D. thesis, Université de Dijon, 1975.

Maritan, A., Colaiori, F., Flammini, A., Cieplak, M., and Banavar, J. R.: Universality classes of optimal channel networks, Science, 272, 984–986, https://doi.org/10.1126/science.272.5264.984, 1996.

755 Nutbrown, D. A.: Identification of parameters in a linear equation of groundwater flow, Water Resour. Res., 11, 581–588, https://doi.org/10.1029/WR011i004p00581, 1975.

Padilla, A., Pulido-Bosch, A., and Mangin, A.: Relative importance of baseflow and quickflow from hydrographs of karst spring, Groundwater, 32, 267–277, https://doi.org/10.1111/j.1745-6584.1994.tb00641.x, 1994.

Pathania, T., Bottacin-Busolin, A., Rastogi, A. K., and Eldho, T. I.: Simulation of groundwater flow in an unconfined sloping aquifer using 760 the element-free Galerkin method, Water Resour. Manage., 33, 2827–2845, https://doi.org/10.1007/s11269-019-02261-4, 2019.

Pauritsch, M., Birk, S., Wagner, T., Hergarten, S., and Winkler, G.: Analytical approximations of discharge recessions for steeply sloping aquifers in alpine catchments, Water Resour. Res., 51, 8729–8740, https://doi.org/10.1002/2015WR017749, 2015.

Rinaldo, A., Rodriguez-Iturbe, I., Bras, R. L., Ijjasz-Vasquez, E., and Marani, A.: Minimum energy and fractal structures of drainage networks, Water Resour. Res., 28, 2181–2195, https://doi.org/10.1029/92WR00801, 1992.

765 Rodriguez-Iturbe, I., Rinaldo, A., Rigon, R., Bras, R. L., Ijjasz-Vasquez, E., and Marani, A.: Fractal structures as least energy patterns: The case of river networks, Geophys. Res. Lett., 19, 889–892, https://doi.org/10.1029/92GL00938, 1992a.

Rodriguez-Iturbe, I., Rinaldo, A., Rigon, R., Bras, R. L., Marani, A., and Ijjasz-Vasquez, E.: Energy dissipation, runoff production, and the three-dimensional structure of river basins, Water Resour. Res., 28, 1095–1103, https://doi.org/10.1029/91WR03034, 1992b.

Rorabaugh, M. I.: Estimating changes in bank storage and ground-water contribution to streamflow, IAHS Publication, 63, 432–441, 1964.

770 Rupp, D. E. and Selker, J. S.: On the use of the Boussinesq equation for interpreting recession hydrographs from sloping aquifers, Water Resour. Res., 42, W12 421, https://doi.org/10.1029/2006WR005080, 2006.

Savenije, H. H. G.: HESS Opinions: Linking Darcy's equation to the linear reservoir, Hydrol. Earth Syst. Sci., 22, 1911–1916, https://doi.org/10.5194/hess-22-1911-2018, 2018.

Schroers, S., Eiff, O., Kleidon, A., Scherer, U., Wienhöfer, J., and Zehe, E.: Morphological controls on surface runoff: an interpretation of 775 steady-state energy patterns, maximum power states and dissipation regimes within a thermodynamic framework, Hydrol. Earth Syst. Sci., 26, 3125–3150, https://doi.org/10.5194/hess-26-3125-2022, 2022.

Sherman, L. K.: Stream flow from rainfall by the unit graph method, Engineering News-Record, 108, 501–505, 1932.

Strüven, J. and Hergarten, S.: Flow recession behavior of preferential subsurface flow patterns, https://doi.org/10.5281/zenodo.7050521, 2022.

780 West, G. B., Brown, J. H., and Enquist, B. J.: A general model for the origin of allometric scaling laws in biology, Science, 276, 122–126, https://doi.org/10.1126/science.276.5309.122, 1997.

West, G. B., Brown, J. H., and Enquist, B. J.: A general model for the structure and allometry of plant vascular systems, Nature, 400, 664–667, https://doi.org/10.1038/23251, 1999a.

West, G. B., Brown, J. H., and Enquist, B. J.: The fourth dimension of life: fractal geometry and allometric scaling of organisms, Science, 284, 1677–1679, https://doi.org/10.1126/science.284.5420.1677, 1999b.

Westhoff, M. C. and Zehe, E.: Maximum entropy production: can it be used to constrain conceptual hydrological models?, Hydrol. Earth Syst. Sci., 17, 3141–3157, https://doi.org/10.5194/hess-17-3141-2013, 2013.

Westhoff, M. C., Zehe, E., and Schymanski, S. J.: Importance of temporal variability for hydrological predictions based on the maximum entropy production principle, Geophys. Res. Lett., 41, 67–73, https://doi.org/10.1002/2013GL058533, 2014.

Westhoff, M. C., Erpicum, S., Archambeau, P., Pirotton, M., and Dewals, B.: Maximum energy dissipation to explain velocity fields in shallow reservoirs, J. Hydraul. Res., https://doi.org/10.1080/00221686.2017.1289268, 2017.

Xu, B., Ye, M., Dong, S., Dai, Z., and Pei, Y.: A new model for simulating spring discharge recession and estimating effective porosity of karst aquifers, J. Hydrol., 562, 609–622, https://doi.org/10.1016/j.jhydrol.2018.05.039, 2018.

Zehe, E., Blume, T., and Blöschl, G.: The principle of maximum energy dissipation: a novel thermodynamic perspective on rapid water flow in connected soil structures, Philos. T. Roy. Soc. B, 365, 1377–1386, https://doi.org/10.1098/rstb.2009.0308, 2010.

Zehe, E., Ehret, U., Blume, T., Kleidon, A., Scherer, U., and Westhoff, M.: A thermodynamic approach to link self-organization, preferential flow and rainfall–runoff behaviour, Hydrol. Earth Syst. Sci., 17, 4297–4322, https://doi.org/10.5194/hess-17-4297-2013, 2013.

Zehe, E., Loritz, R., Edery, Y., and Berkowitz, B.: Preferential pathways for fluid and solutes in heterogeneous groundwater systems: self-organization, entropy, work, Hydrol. Earth Syst. Sci., 25, 5337–5353, https://doi.org/10.5194/hess-25-5337-2021, 2021.

Zhao, J., Wang, D., Yang, H., and Sivapalan, M.: Unifying catchment water balance models for different time scales through the maximum entropy production principle, Water Resour. Res., 52, 7503–7512, https://doi.org/10.1002/2016WR018977, 2016.